

Manuscript number DOI:10.1002/ppap.

Article type: Full Paper

Turbulence and entrainment in an atmospheric pressure dielectric barrier plasma jet.

Y. Morabit¹, R. D. Whalley², E. Robert³, M. I. Hasan¹ & J. L. Walsh^{1*}

¹ Centre for Plasma Microbiology, Department of Electrical Engineering & Electronics, University of Liverpool, L69 3GJ, UK.

² School of Mechanical and Systems Engineering, Newcastle University, NE1 7RU, UK.

³ GREMI UMR 7344 CNRS/Université d'Orléans, Orléans, 45067, France.

Abstract

Particle Image Velocimetry, Laser-Induced Fluorescence, and computational modeling are used to quantify the impact of plasma generation on air entrainment into a helium plasma jet. It is demonstrated that discharge generation yields a minor increase in the exit velocity of the gas. In contrast, the laminar to turbulent transition point is strongly affected, attributed to an increase in plasma-induced perturbations within the jet shear layer. The temporal decay of laser-induced fluorescence from OH is used as an indicator for humid air within the plasma. The results show that plasma-induced perturbations increase the quenching rate of the OH fluorescent state; indicating shear layer instabilities play a major role in determining the physicochemical characteristics of the plasma.

*Corresponding author: jlwalsh@liverpool.ac.uk

1 Introduction

Atmospheric pressure plasma jets have been widely used in many healthcare and materials processing applications, ranging from etching and deposition to microbial decontamination and cancer therapy.^[1-5] Perhaps the most widely used plasma jet configuration is based on the dielectric barrier discharge employing a noble gas such as helium or argon; typically, the gas is flushed through a dielectric capillary and subjected to an applied voltage using one or more electrodes placed inside and/or outside of the capillary. On application of a time-varying voltage of sufficient magnitude to cause breakdown, a discharge forms within the capillary and propagates as a fast-moving ionization wave along the noble gas channel, ultimately exiting the capillary and extending into the surrounding quiescent air. From an application perspective, atmospheric pressure plasma-based applications typically rely on reactive oxygen and nitrogen species (RONS), many of which are created through the interaction between the plasma plume and the quiescent air.

A large number of studies have considered the impact that plasma generation has on the characteristics of the flowing noble gas. It has been widely reported that the generation of plasma in a buoyant axisymmetric jet configuration leads to a rapid transition from laminar to turbulent flow.^[6-10] It is commonly assumed that gas heating and Electrohydrodynamic (EHD) forces play a role in creating turbulence within the flowing gas channel, with the latter being considered as the dominant mechanism. Indeed, Park et al. used a pulsed plasma jet to demonstrate that EHD forces are primarily exerted by space charge drifting in the applied electric field following streamer propagation, confirming the modelling results of Hasan and colleagues.^[11, 12] Whalley and Walsh demonstrated that the spatially developing velocity fields in an inhomogeneous axisymmetric plasma jet flow are turbulent and self-similar, with characteristics matching the turbulent velocity fields which develop naturally with increasing distance from the jet exit. Using an order-of-magnitude analysis, it was predicted that the presence of a discharge should only increase the jet exit velocity by approximately 10%.^[8] Many works in the field of fluid dynamics have indicated

27 that the generation of turbulence in an axisymmetric jet flow is related to small-amplitude body
28 forces causing perturbations in the unstable shear layers at the jet exit, which grow as they move
29 downstream.^[13- 17]
30

31 To characterize the chemical species produced downstream of the jet orifice, multiple invasive and
32 non-invasive diagnostic techniques have been applied, including tuneable diode laser absorption
33 spectroscopy (TDLAS),^[18] mass spectroscopy (MS),^[19] Fourier transform infrared spectroscopy
34 (FTIR),^[16] Laser-Induced Fluorescence (LIF) and Two-photon Absorption Laser-Induced
35 Fluorescence (TALIF).^[21-23] Of all the techniques investigated, LIF based methods are particularly
36 convenient as they provide the high spatiotemporal resolution required to accurately investigate the
37 complex downstream chemistry in a plasma jet while facilitating the quantification of absolute
38 radical densities. Regardless of the diagnostic technique used, it is clear that a significant proportion
39 of the reactive chemical species produced within the downstream region of the jet are a result of
40 reactions between the noble gas plasma and molecular gas impurities entrained from the
41 surrounding environment, which is typically humid air. Given that the interplay between the
42 propagating plasma plume and ambient environment has a considerable impact on the
43 physicochemical properties of the plasma jet and, therefore, on the application efficacy,
44 understanding the underpinning mechanisms of how air becomes entrained within the flowing noble
45 gas channel is of vital importance.

46
47 This study investigates the entrainment of air into a helium plasma jet and explores the hypothesis
48 that small perturbations within the jet shear layer resulting from plasma generation not only result in
49 the early onset of turbulence but also act to increase entrainment of air into the laminar region of the
50 jet. Particle image velocimetry (PIV) was used to quantify the fluid dynamics of the helium jet flow
51 beyond the jet orifice and combined with LIF to provide a sensitive means of assessing the
52 entrainment of humid air into the discharge.

53

54 **2 Experimental and computational methods**

55 **2.1 Plasma Jet and PIV setup**

56 The plasma jet used in this study comprised of a quartz capillary with an inner diameter D , equal to
57 3 mm and an outer diameter of 5 mm, a metallic strip was wrapped around the outer diameter of the
58 capillary to act as a ground electrode, as shown in **Figure 1**. A tungsten pin was positioned
59 coaxially within the quartz capillary and connected to a high-voltage sinusoidal power source
60 operating at a frequency of 20 kHz. Two applied voltage cases were examined in this study, 14
61 kVpp and 10 kVpp, with the latter being just above the point of gas breakdown. Helium gas with a
62 purity of 99.999% was flushed through the capillary at 2 Standard Liters per Minute (SLM), giving
63 a maximum exit velocity, U_m , equal to 9.4 m s^{-1} .

64

65 To quantify the flow field created by the plasma jet, PIV measurements were undertaken using the
66 experimental setup shown in Figure 1. The plasma jet was inserted into a large sealed chamber
67 (volume $> 2 \text{ m}^3$), which was seeded using oil droplets with a nominal size of $1 \text{ }\mu\text{m}$. The chamber
68 ensured that the plasma jet flow was not influenced by any external draughts. A similar
69 experimental arrangement was used in the previous works of the authors,^[8] where it was observed
70 that an insufficient number of seeding particles were entrained within the laminar region of the jet
71 to obtain reliable PIV measurements. To overcome this challenge, the helium flow into the jet
72 capillary was seeded using oil droplets, which also had a nominal size of $1 \text{ }\mu\text{m}$. The addition of oil
73 droplets to the helium gas flow has an obvious potential to disrupt the discharge; while such
74 changes are difficult to assess, the breakdown voltage and length of plasma plume were found not
75 to change significantly. Furthermore, Rayleigh scattering was used to obtain an approximate
76 indication of the laminar region length in an un-seeded jet and a close agreement was observed
77 when compared to the PIV measurements on the seeded jet, suggesting the presence of the seeding
78 particles had a minimal impact on the fluid dynamic properties of the system. Given the nominal

size of the seeding particles, the Stokes number was found to be less than 0.1, thus ensuring that the particles followed the fluid flow closely with tracing errors being $< 1\%$.^[24]

Planar velocity measurements were conducted using a 2D particle image velocimetry system from TSI inc. The system consisted of a double pulsed Nd:YLF laser operating at 200 Hz with a pulse duration of 100 ns at a wavelength of 527 nm and was used to generate a 1 mm thick light sheet that was projected into the seeding chamber and across the plasma jet orifice. A high-speed Phantom Miro Lab 340 camera was positioned outside the seeding chamber normal to the laser sheet and synchronized with the laser such that each frame captured a single laser pulse. A spatial calibration was performed and the time delay between consecutive laser pulses (Δt) was set to 30 μs , a value chosen to capture the movement of oil droplets over a grid with spatial dimensions of 350 μm^2 , enabling the velocity vectors to be computed using a recursive cross-correlation technique. For each measurement condition, the plasma jet was operated for several seconds before data capture to ensure steady-state conditions were achieved. Each dataset comprised of 800 frames that were used to make 400 individual velocity vector maps; in the case of time-averaged measurements, all 400 vector maps were averaged and presented as a single figure.

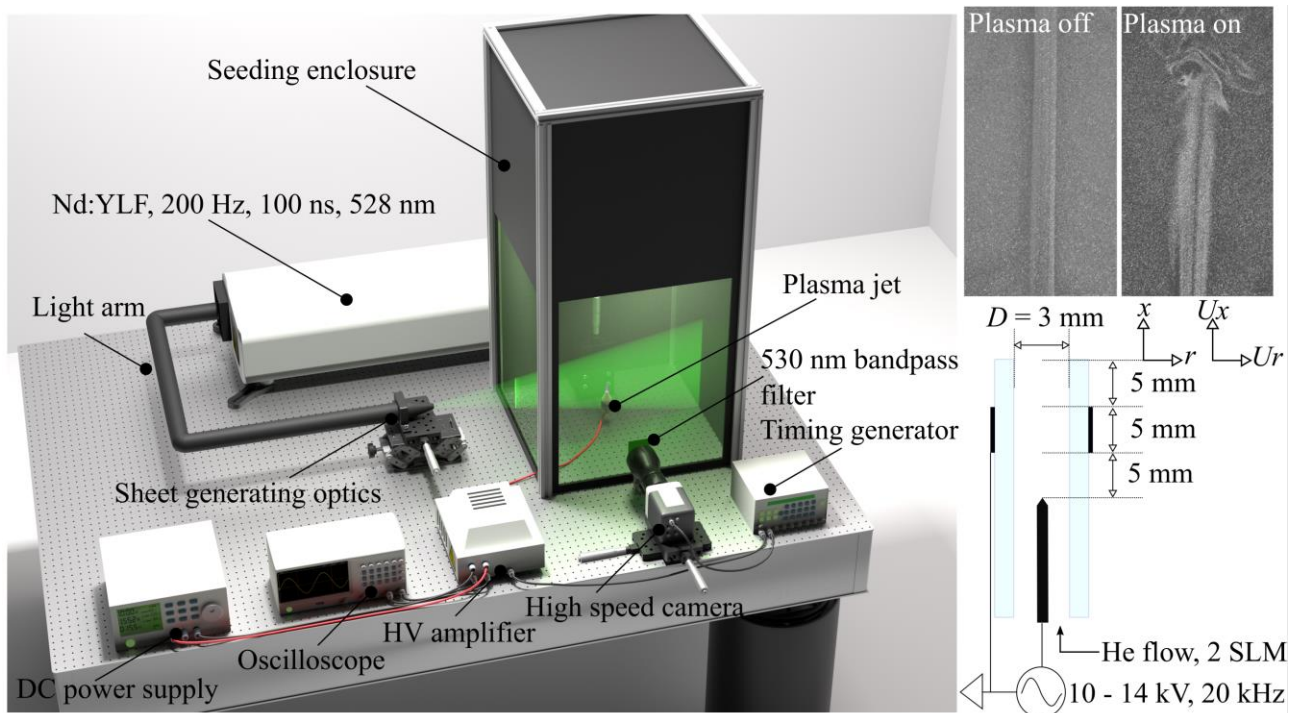


Figure 1. Diagram showing the layout of the particle image velocimetry experiment and

configuration of the plasma jet device, with representative PIV images for the plasma off and

plasma on cases, vectors U_x and U_r represent the axial and radial velocity components, respectively.

2.2 LIF setup and OH density calibration

The LIF measurement system used in the investigation is shown in **Figure 2**, the system was used to measure OH radical density and to obtain an indication of air entrainment within the plasma plume through the measurement of the radiative decay time of the laser-excited OH(A) state. The system comprised of a tuneable dye laser (Sirah Cobra Stretch with second harmonic generation unit) pumped by a 6 ns pulsed Nd:YAG laser with a wavelength of 532 nm, pulse energy of 120 mJ and a repetition rate of 10 Hz. A number of LIF excitation schemes have been proposed for the measurement of OH radicals in atmospheric pressure plasmas.^[25-27] In this work, the dye laser was tuned to generate an output at a wavelength 282.58 nm to excite the $P_1(2)$ transition from the $f_1(2)$ rotational level of OH X($v'' = 0$) to the $F_1(1)$ rotational level of OH A($v' = 1$). A number of previous studies have used a similar excitation scheme due to the $P_1(2)$ transition being spectrally separated from adjacent lines and the $f_1(2)$ level having the largest relative population in the temperature range under investigation.^[28]

The 282.58 nm beam emitted from the dye laser was measured to have a pulse energy in excess of 17 mJ, a value several orders of magnitude above the range linear LIF measurements are typically made (1 – 10 μ J).^[29] Operation beyond the linear region greatly complicates the interpretation of the results, as the ground rotational level is significantly depleted by light absorption and partially refilled by fast rotational redistribution, altering the LIF outcome dependent on the unknown gas composition and temperature. To attenuate the laser energy to a suitable range an optical arrangement similar to that employed by Ries et al. was adopted,^[21] two quartz plates were angled to split the beam as shown in Figure 2, with a small fraction being reflected towards the plasma jet

122 and the majority of the beam passing through to beam dumps mounted behind each plate. Following
123 attenuation, the beam was directed through an uncoated quartz plano-convex lens with a focal
124 length of 1 m, and a pinhole of 1 mm was positioned to act as a spatial filter, further attenuating the
125 beam. Using this approach, the maximum laser pulse energy was found to be approximately 15 μJ ;
126 small changes to the Q-switch delay of the pump laser were subsequently used to vary the pulse
127 energy between 1 and 15 μJ . Laser power was measured using a Thorlabs PM100D optical power
128 and energy meter equipped with a thermal volume absorber power sensor.

129

130 To capture the fluorescence of excited OH molecules, an Andor iStar740 iCCD camera was fitted
131 with a Jenoptik UV 105 mm f/4.5 imaging lens. The camera arrangement was positioned to face the
132 plasma jet perpendicular to the laser beam. For each image recorded, the iCCD camera was
133 configured to accumulatively capture 500 laser pulses, using an optical gate width equal to 8 ns for
134 each exposure. Following the approach of Verreycken et al.,^[28] no bandpass filter was used during
135 LIF measurements to avoid the need for additional corrections in the calibration procedure. A
136 consequence of this approach is the potential for interference of the fluorescent signal from other
137 emissions within the plasma and the Rayleigh scattering signal. A background subtraction of the
138 emission captured with the plasma energized and laser de-tuned was used to correct for light
139 emitted by the plasma and any scattered light. To ensure the measurements were conducted within
140 the linear LIF region, the measured LIF intensity was plotted against laser energy and a linear fit
141 applied. It was determined that the linear range was between 1 μJ to 10 μJ , a value in close
142 agreement with several past LIF investigations.^[21, 28]

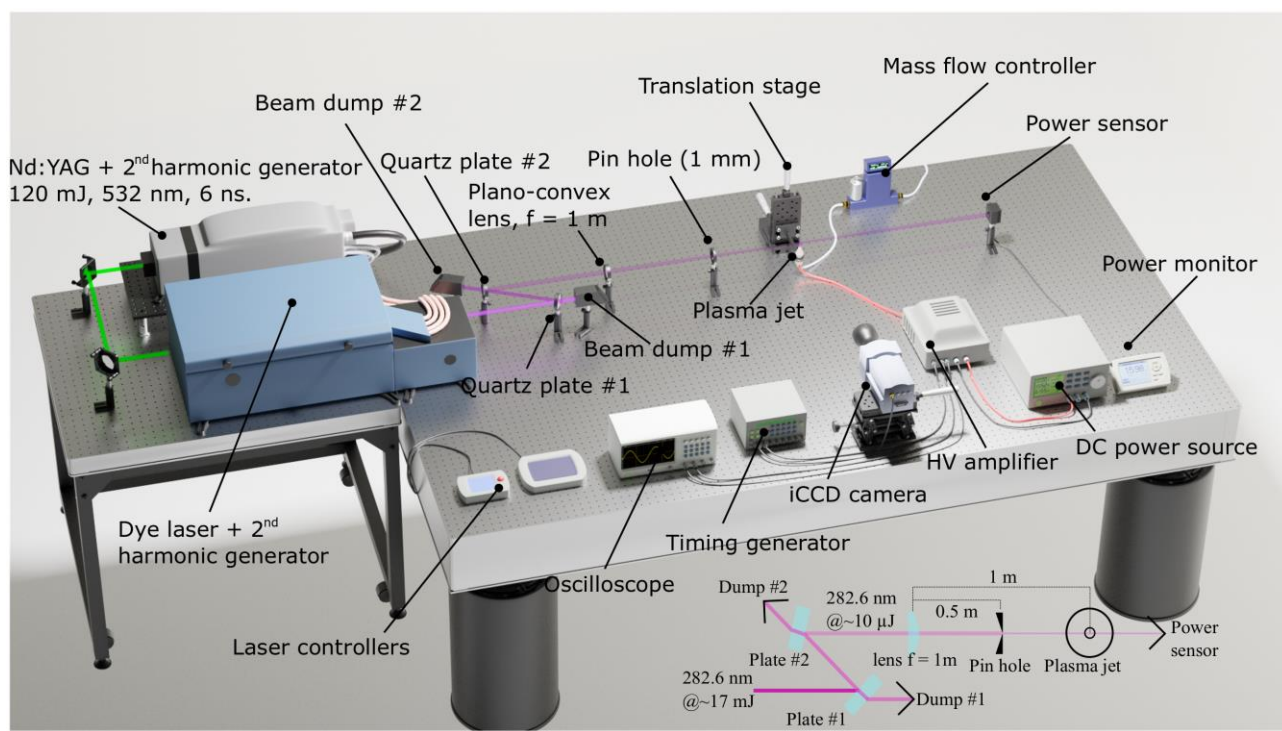


Figure 2. Diagram showing the layout of the Laser-Induced Fluorescence experiment, insert highlights optical arrangement used to achieve a three-order reduction in laser intensity.

Absolute calibration of the LIF signal to determine the density of ground-state OH can be achieved via several methods, including UV absorption, chemical modeling, and Rayleigh scattering.^[28, 30] In this investigation, the Rayleigh scattering approach was adopted due to its high degree of accuracy, and a similar methodology to that described by Verreycken et al. was adopted.^[28] Calibration by Rayleigh scattering requires detailed knowledge of the rotational and vibrational energy transfer rates, which vary significantly depending on the nature of the quenchers present; thus an accurate appreciation of the gas composition is essential. Careful consideration must be applied in the case of a plasma jet as the gas composition varies as a function of distance from the jet orifice; further details on this are provided in section 2.3. Also important for the determination of absolute OH density is the decay time of the laser-excited fluorescent state. This was measured at each spatial position by applying a time delay to the iCCD camera from 6 ns (*i.e.*, immediately after the laser pulse) up to 2000 ns; at each time point the fluorescent intensity from 500 laser shots was accumulated to form a single image. From each image, the sum of LIF intensity in a 0.36 mm^2

interrogation area on the jet centreline was determined and plotted as a function of delay time, an exponential fit was applied to determine the decay rate at each spatial position.

In addition to the gas composition, the gas temperature can also affect the interpretation of the LIF data. To investigate the influence of plasma generation on gas temperature, an Omega FOB100 fiber-optic thermometer was used, the dielectric temperature probe was positioned in the plasma at various points downstream of the jet orifice and the temperature recorded. The temperature was found to vary little with spatial position, with a maximum of 10 K above ambient located close to the capillary orifice, such observations are in-line with previous studies.^[8]

The remainder of the calibration process closely followed that reported previously by Verreycken et al. and will only be summarized in brief here.^[28] To obtain Rayleigh scattering data for calibration, the jet capillary was supplied with Nitrogen gas at a flow rate of 2 SLM, while not strictly necessary, the nitrogen flow helped to ensure dust from the ambient environment did not enter the measurement region of interest. The laser power was varied from 2 to 15 μJ in 1 μJ increments, and the sum of the Rayleigh scattered signal intensity in a square region of interest measuring 0.36 mm^2 was calculated. The measured Rayleigh scattered signal, S_{Ray} (#counts), can be written as:

$$S_{Ray} = \eta N_n \frac{\partial^{\beta=0} \sigma_0}{\partial \Omega} V_{Ray} I_L t_L \quad (1)$$

Where η is the calibration constant (#counts sr J^{-1}), N_n is the density of scattering particles (m^{-3}), $\partial^{\beta=0} \sigma_0 / \partial \Omega$ is the differential cross-section for Rayleigh scattering ($\text{m}^2 \text{sr}^{-1}$), V_{Ray} is the volume from which Rayleigh scattering is collected (m^3), I_L is the laser irradiance (W m^{-2}) and t_L is the temporal length of the laser pulse (s), which was measured by replacing the power meter shown in Figure 2 with a fast photodetector. After considering the non-uniformity of the laser energy density, Equation (1) becomes:

$$S_{Ray} = \eta N_n \frac{\partial^{\beta=0} \sigma_0}{\partial \Omega} E_L \Delta x \quad (2)$$

186

187 Where E_L is the laser energy (J), and Δx is the length of the detection volume (m). Following this,
188 the calibration constant η was obtained from the slope α , of the measured Rayleigh intensity as a
189 function of laser energy multiplied by pressure:

190

$$\eta = \alpha k_B T \frac{\partial^{\beta=0} \sigma_0}{\partial \Omega} \Delta x \quad (3)$$

192

193 Where k_B is the Boltzmann constant and T is the temperature (K). Using the calibration factor, the
194 intensity of the laser-induced fluorescence S_{LIF} , can be expressed as:

195

$$S_{LIF} = \frac{1}{4\pi} \int \eta E n_{exc}(x, y, z, t) A \, dx dy dz dt \quad (4)$$

197

198 Where E is the energy gap according to the chosen transition, A is the Einstein emission coefficient
199 (s^{-1}), and $n_{exc}(x, y, z, t)$ is the density of OH in the excited state. To determine the ground state OH
200 density based on n_{exc} in Equation (4), the 4-level collisional radiative model reported by Verreycken
201 et al. was utilized.^[28] Briefly, the model follows the densities of 3 laser-excited levels of OH in
202 addition to the ground state. The followed levels are the ground state OH X($v''=0$), OH A($v'=1$),
203 OH A($v'=0$), and OH X($v''=1$). For each level an ordinary differential equation is solved describing
204 the gains and the losses of that level, leading to a coupled system of 4 equations. The processes
205 described in the system are the radiative excitation by the laser, the quenching by air constituents,
206 and the vibrational relaxation. It is assumed in the model that the rotational energy transfer is much
207 faster than the other processes; thus, the rotational levels are not resolved. The inputs to the 4-level
208 model include the experimental parameters listed in **Table 1**, the gas composition determined by the
209 flow model described in section 2.3, and an estimated ground state OH density. Solving the 4-level
210 model provides a prediction of the LIF signal intensity, which by comparison to the measured LIF
211 signal intensity is used to determine the actual ground-state OH density. Full details of the

implementation can be found in the works of Verreycken and colleagues.^[28] Finally, Table 1 shows the relevant experimental parameters used in the LIF measurements, and these were also used as inputs for the computational model.

215

Table 1. Experimental parameters used in LIF measurements and absolute density calibration

Parameter	Description	Value
λ_L	Laser wavelength	282.58 [nm]
$\Delta\lambda_L$	Linewidth of the laser	0.95 [pm]
g_{int}	Overlap integral	0.017 [m]
A_L	Area of the laser beam	0.0746 [mm ²]
E_L	Laser energy per pulse	10 [μJ]
τ_L	Temporal FWHM of the laser pulse	6 [ns]
Δx	Length of the detection volume	0.359 [mm]
Δy	Width of the detection volume	0.359 [mm]
Δs	The spatial FWHM of the laser beam at the observation point	0.1795 [mm]

217

218

2.3 Computational model and statistical analysis methodology

To account for the varying composition of gas downstream of the jet orifice, a computational model was developed that solved for the velocity field of the gas mixture in addition to the mass fractions of its constituents, namely N₂, O₂, H₂O, and He. To obtain the velocity field, the model solved the mass continuity Equation (5), which solves for the mass density of the entire gas mixture, and the momentum conservation Equation (6). To compute the densities of the species constituting the gas mixture, the continuity equation, given by Equation (7), was solved for the mass fraction of three species, while the mass fraction of the fourth was determined from the pressure constraint. All equations were solved in steady-state mode (*i.e.*, time-independent equations):

$$\nabla \cdot (\rho \vec{u}) = 0 \quad (5)$$

$$\rho(\vec{u} \cdot \nabla) \vec{u} = -\nabla p + \nabla \cdot \left(\mu(\nabla \vec{u} + \nabla \vec{u}^T) - \frac{2}{3} \mu(\nabla \cdot \vec{u}) I \right) - (\rho - \rho_0) g \quad (6)$$

$$\rho(\vec{u} \cdot \nabla) \omega_i + \nabla \cdot (\vec{\Gamma}_i) = 0 \quad (7)$$

231 Where ρ is the density of the gas mixture (kg m^{-3}), \vec{u} is the velocity field of the gas mixture (m s^{-1}),
 232 p is the gas mixture's pressure (Pa), μ is the gas mixture's viscosity (Pa s), I is the identity matrix,
 233 ρ_0 is the density of air (kg m^{-3}), and g is the gravitational constant (m s^{-2}), ω_i is the mass fraction of
 234 the i^{th} species, and Γ_i is the diffusive flux of the i^{th} species, which is calculated according to
 235 Maxwell-Stefan theory for diffusion as given by Equation (8 - 10).^[31, 32]

$$236 \quad \vec{\Gamma}_i = \rho \omega_i \vec{V}_i \quad (8)$$

$$237 \quad \nabla x_i = \sum_{j=1}^4 \frac{x_i x_j}{D_{ij}} (\vec{V}_j - \vec{V}_i) + \frac{\nabla p}{p} (\omega_i - x_i) \quad (9)$$

$$238 \quad x_i = \frac{M_n}{M_i} \omega_i \quad (10)$$

239 Where \vec{V}_i is the diffusion velocity of the i^{th} species (m s^{-1}), x_i is the mole fraction of the i^{th} species
 240 (dimensionless), which is related to the mass fraction by Equation (8), and D_{ij} is the binary
 241 diffusion coefficients between the i^{th} and the j^{th} species ($\text{m}^2 \text{s}^{-1}$). A list of the binary diffusion
 242 coefficients used in the model is given in **Table 2**. It should be noted that Equation (9) is
 243 incorporated in the model as a constraint linking the flux term and the mass fraction term in
 244 Equation (7). In Equation (10), M_i and M_n are the molecular weight of the i^{th} species and the average
 245 molecular weight, respectively (kg mol^{-1}). Lastly, the computational domain and the boundary
 246 conditions used are described in the supplementary information.

247

248 *Table 2.* A list of binary diffusion coefficients used in the model.

Combination	Diffusion coefficient [$\text{m}^2 \text{s}^{-1}$]	Reference
N ₂ – He	6.78×10^{-5}	[33]
N ₂ – O ₂	2.09×10^{-5}	[34]
N ₂ – H ₂ O	2.54×10^{-5}	[35]
O ₂ – He	7.36×10^{-5}	[33]
He – H ₂ O	8.36×10^{-5}	[35]
O ₂ – H ₂ O	3.185×10^{-5}	[35]

249

250 As stated in the introduction section, it is hypothesized that plasma-induced turbulence affects the
 251 flow's velocity field and thus the gas composition. To account for such effects in the computational

252 model, the Reynolds-Averaged Navier-Stokes (RANS) approach for modeling turbulence was
 253 followed, where a turbulent viscosity μ_T (also known as eddy viscosity) was added to the viscosity
 254 of the gas mixture. The eddy viscosity is a mathematical means to describe the loss of momentum
 255 of the flow as a result of turbulence as an “effective” viscosity that is added to the physical viscosity
 256 of the fluid. Similarly, a turbulent diffusivity D_T is added to the binary diffusion coefficients.^[32] The
 257 computation of the eddy viscosity is typically done using one of the conventional RANS turbulence
 258 models, such as the $k - \varepsilon$ model. Considering that such models were calibrated for flows without
 259 plasma, their use for plasma modified flows will yield results with unknown accuracy. To overcome
 260 this challenge, statistical analysis of the PIV data was conducted to obtain the necessary parameters
 261 to calculate the eddy viscosity resulting from the plasma generation. Following the $k - \varepsilon$ modeling
 262 approach, the turbulent kinetic energy k ($\text{m}^2 \text{s}^{-2}$) and the turbulent kinetic energy dissipation rate ε
 263 ($\text{m}^2 \text{s}^{-3}$) are defined by Equation (11) and (12).^[36]

$$264 \quad k = \frac{1}{2} \left(\overline{u_r'^2} + \overline{u_x'^2} \right) \quad (11)$$

$$265 \quad \varepsilon = 2\nu \overline{s_{ij}' \cdot s_{ij}'} \quad (12)$$

266 Where u_r' and u_x' are the time fluctuating velocity field components with respect to the average
 267 velocity field, which were calculated from PIV data by subtracting the time-averaged velocity field
 268 from each of the 400 instantaneous velocity maps captured during a measurement, then averaging
 269 the square of these fluctuations. In Equation (12), ν is the kinematic viscosity ($\text{m}^2 \text{s}^{-1}$), and s_{ij}' is the
 270 fluctuating deformation rate of the fluid (s^{-1}), which was calculated from the PIV data as outlined by
 271 Xu and colleagues.^[37] After calculating k and ε the eddy viscosity was calculated according to
 272 Equation (13).^[36]

$$273 \quad \mu_T = \rho C \frac{k^2}{\varepsilon} \quad (13)$$

274 Where C is a constant equal to 0.0016 and ρ is the self-consistent gas mixture density calculated by
 275 the model. The turbulent diffusivity D_T is related to the eddy viscosity by Equation (14).^[28]

$$276 \quad D_T = \frac{\mu_T}{\rho S c_T} \quad (14)$$

277 Where Sc_T is the turbulent Schmidt number, obtaining an accurate value for this in a plasma-
278 modified flow is not possible; however, the turbulent Schmidt number is close to unity for a wide
279 variety of gas flows under very diverse conditions; hence it is assumed to be 1 in this
280 investigation.^[38] The model was subsequently solved with the experimental input of μ_T and D_T ,
281 which were smoothed and mirrored, then added to their physical counterpart quantities. The model
282 was solved for both applied voltage cases investigated in this work, in addition to an unperturbed
283 laminar case, where the eddy viscosity and diffusivity were set to zero.

284
285 As described in section 2.2, the radiative collisional model consisted of a system of Ordinary
286 Differential Equations (ODE) describing the LIF transitions. The system was solved at every point
287 in the computational domain close to the jet's orifice ($x < 20$ mm, $x/D < 7$), with the gas
288 composition required for the ODEs being taken from that calculated by the fluid flow model. To
289 quantify the density of ground-state OH, the 4-level model reported by Verreycken et al. was
290 adopted.^[28] To validate the developed computational model, the predicted LIF signal decay times
291 were compared to those measured experimentally at multiple points along the jet axis; a close
292 agreement was observed and is further discussed in the results section.

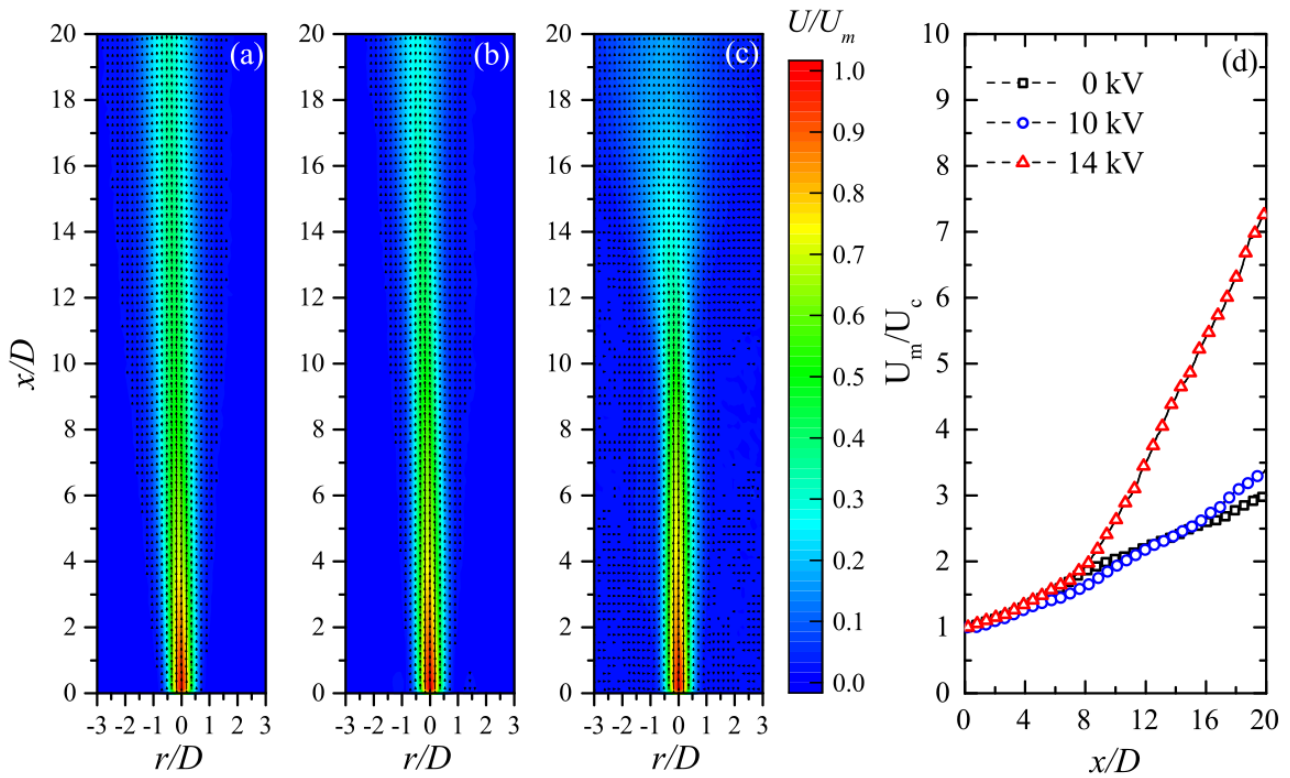
294 **3 Results and discussion**

295 **3.1 Influence of plasma on jet velocity and turbulence generation**

296 PIV measurements were undertaken to quantify the velocity of the flowing helium gas and the
297 resulting perturbation of the surrounding quiescent air beyond the jet orifice. **Figure 3** (a-c) shows
298 the ensemble-averaged two-component velocity vector maps and velocity magnitude (U)
299 normalized to the measured exit velocity (U_m) for the 0 kV, 10 kV, and 14 kV cases, respectively.
300 Without a plasma discharge (0 kV case), the undisturbed helium flow appeared laminar over the
301 entire measurement region, confirmed by the ensemble-averaged centerline velocity (U_c) profile in
302 Figure 3(d). On the application of a 10 kV sinusoidal waveform, a weak discharge was observed to

303 form, indicating gas breakdown had been achieved; under such conditions, little obvious change to
 304 the velocity profile was observed. An increase in applied voltage from 10 kV to 14 kV led to an
 305 increase in the length of the visible plasma plume. Comparing Figure 3(b) and 3(c) highlights the
 306 impact of the applied voltage on the flow structure downstream of the jet orifice, with the higher
 307 applied voltage resulting in a significant reduction in the length of the laminar flow region. From
 308 the ensemble-averaged centerline velocity, an abrupt change in gradient is observed at
 309 approximately $8 x/D$, indicating a transition to turbulence. While such results are perhaps the first
 310 quantitative measurements of velocity within a plasma jet, they are highly consistent with previous
 311 observations made using qualitative methods such as Schlieren imaging. ^[9, 39]

312



313

314 **Figure 3.** Ensemble averaged particle image velocimetry measurements of the plasma jet obtained
 315 at applied voltages of (a) 0 kV, (b) 10 kV, and (c) 14 kV, (d) shows the reciprocal of the ensemble-
 316 averaged centerline velocity (U_c) normalized to the measured exit velocity (U_m).

317

318 In absolute terms, the generation of plasma with an applied voltage of 14 kV was found to increase
319 U_m by 0.94 m s^{-1} , representing a relatively modest increase of approximately 10% compared to the 0
320 kV case. Such increases in velocity are in line with those predicted by others and are a consequence
321 of gas heating and electrohydrodynamic forces induced by the plasma, with the latter mechanism
322 being the most likely dominant factor.^[8, 11] Notably, the modest change in velocity associated with
323 plasma generation cannot directly explain the transition to turbulence observed when comparing
324 Figure 3(a) and 3(c). Past studies on turbulence generation in axisymmetric round jets have revealed
325 that turbulence initiates due to instabilities within the shear layers at the jet exit that become
326 amplified as they travel downstream.^[13-17] As the instabilities grow, they cause velocity fluctuations,
327 Reynolds shear stresses, and thus the production of turbulence.^[8] Many previous studies have
328 explored ‘excited’ jets that employ alternative means to perturb the jet flow in order to investigate
329 the mechanisms of turbulence generation.^[40-45] For example, the impact of sonic excitation on the
330 jet velocity profile shows a remarkable similarity to those observed in this study^[41]; hence it is
331 posited that plasma generation is an alternative means to excite an axisymmetric round jet, resulting
332 in the rapid onset of turbulence through increased shear layer instability with little change to
333 velocity.

334

335 While the growth of small-scale instabilities within the jet shear layer has a significant impact on
336 the laminar to turbulent transition, they also provide a mechanism to enhance entrainment of
337 quiescent air into the laminar region of the plasma jet.^[45] To investigate the influence of plasma
338 generation on instabilities in the jet shear layer, the eddy viscosity μ_T was calculated. The eddy
339 viscosity profiles for the two plasma cases investigated in this work are shown in **Figure 4** (a-b).
340 Three characteristic zones can be observed within the profiles, the first is close to the jet orifice,
341 where a region of low μ_T exists, which can be explained by the fact that this is the laminar region
342 where the amplitude of velocity fluctuations is small, leading to low turbulent kinetic energy k , and
343 consequently, a low μ_T as Equation (13) shows. The second zone (e.g., $4 - 10 x/D$ in Figure 4(b))

344 coincides with the transition region, as inferred from Figure 3(d), where the value of μ_T peaks. This
345 is attributed to the large scale fluctuations/eddies starting to appear in the transition region, leading
346 to high turbulent kinetic energy k , considering that such large fluctuations live long enough to be
347 transported downstream, the dissipation rate of the turbulent energy ε is relatively low in this
348 region, thus leading to a peak of μ_T as follows from Equation (13). The third zone (e.g. $> 10 x/D$ in
349 Figure 4(b)) coincides with the turbulent region, as inferred from Figure 3(d), which has a moderate
350 value of μ_T . As known from the energy cascade theory of turbulence,^[46] the large eddies generated
351 in the transition region break into smaller eddies in the fully turbulent region, the small eddies are
352 dissipated into heat due to the physical viscosity of the fluid.^[46] In this sense, the turbulent kinetic
353 energy k is high, while the turbulent dissipation rate ε is also high, leading to a moderate value of μ_T .
354 From Figure 4(a-b), it is clear that the eddy viscosity for the 14 kV case has a larger magnitude
355 compared to the 10 kV case, which is consistent with the PIV results presented in Figure 3(b-c).
356 When comparing the average value of μ_T in zone one ($x/D < 4$) for both cases it is found that μ_T for
357 the 10 kV case is approximately 70%-80% of that for the 14 kV case, indicating that the plasma's
358 perturbation to the flow in the laminar region is more significant for the 14 kV case in comparison
359 to the 10 kV case.

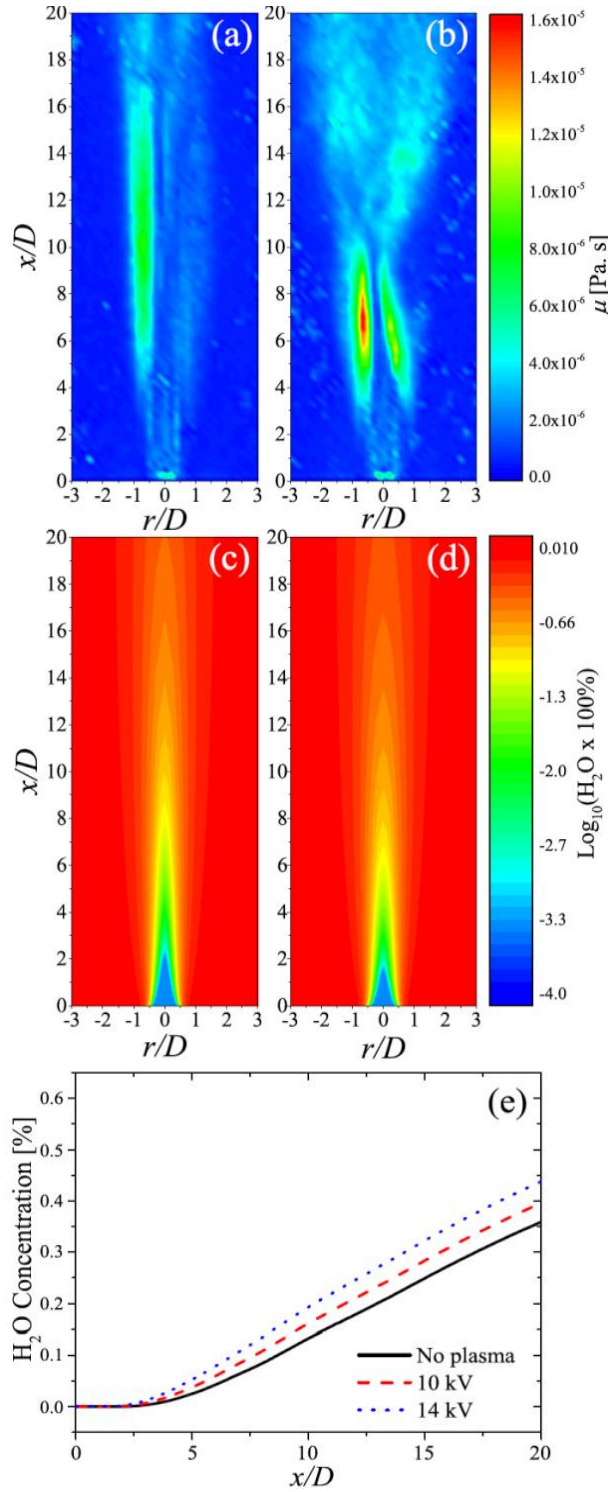


Figure 4. Eddy viscosity calculated from PIV measurements for the (a) 10 kV and (b) 14 kV excited plasma jet and the calculated percentage of H_2O in the helium flow under (c) 0 kV and (d) 14 kV conditions; (e) shows the percentage of H_2O along the jet centerline for all three cases.

As described in section 2.3, a higher value of the eddy viscosity of μ_t indicates a higher value of eddy diffusivity D_T , which adds to the physical diffusion coefficients, leading to increased

367 entrainment of air into the helium jet for higher values of μ_T . To highlight the impact of the plasma-
368 induced entrainment, Figure 4 (c) and (d) show the computed percentage of H₂O in the gas mixture
369 for the 0 kV and 14 kV cases, respectively. Notably, the 0 kV case represents an unperturbed
370 laminar flow where quiescent air is entrained due to the physical diffusion only. While in the case
371 of the perturbed flow shown in Figure 4(d), air entrainment occurs due to physical diffusion plus the
372 “effective” eddy diffusion due to turbulence. The centerline concentration of H₂O, shown in Figure
373 4 (e), was set to 0.00004% for all cases, a value obtained from the helium gas provider. Moving
374 downstream to 2 x/D, the level of H₂O in the unperturbed 0 kV case was found to increase to be
375 approximately 0.0005 %. In contrast, the H₂O concentration in the perturbed case was found to be
376 0.0034 %, representing a 7-fold increase. Further downstream at 6 x/D, the H₂O concentration in
377 the unperturbed case was found to be 0.046%, compared to 0.082% in the perturbed case,
378 representing a 1.8-fold increase. When moving downstream, the difference between the unperturbed
379 case and the 14 kV perturbed case diminishes as a result of the increasing density of the gas
380 mixture, which lowers the value of the eddy diffusivity as defined by Equation (4).

381

382 **3.2 OH fluorescence decay rate and absolute density**

383 As described by Yonemori et al. the decay rate of the LIF signal from OH provides a sensitive
384 indication of the helium-air mixing ratio as the quenching rate of the laser-excited state is strongly
385 influenced by the density of quenching species present within the flowing helium gas (e.g., N₂, O₂,
386 H₂O).^[47] In this study, a comparison between the measured LIF decay rate and computed decay rate
387 by the model was used to validate the adopted computational approach describing plasma-induced
388 entrainment, thus enabling the accurate quantification of absolute OH density downstream of the jet
389 exit. The decay time is obtained from the fitting of the temporal evolution of the LIF signal
390 intensity, as described in section 2.3. **Figure 5** shows the measured and computed LIF decay time
391 as a function of downstream spatial position for both the 10 kV and 14 kV cases; additionally, the
392 predicted decay time for a hypothetical unperturbed (laminar) helium flow is shown. The LIF decay

time is shorter at all spatial positions under both 10 and 14 kV excitation compared to what would be observed under idealized laminar conditions. As highlighted in Figure 4 (c) and (d), plasma generation increases air entrainment, which acts to increase the density of quenchers and thus increase the quenching rate of the OH fluorescent state. This result provides experimental evidence supporting the hypothesis that plasma generation increases the entrainment of air within the helium jet at all spatial positions, not just the fully turbulent region. The calculated decay times closely match the measured data points, with both cases showing the agreement.

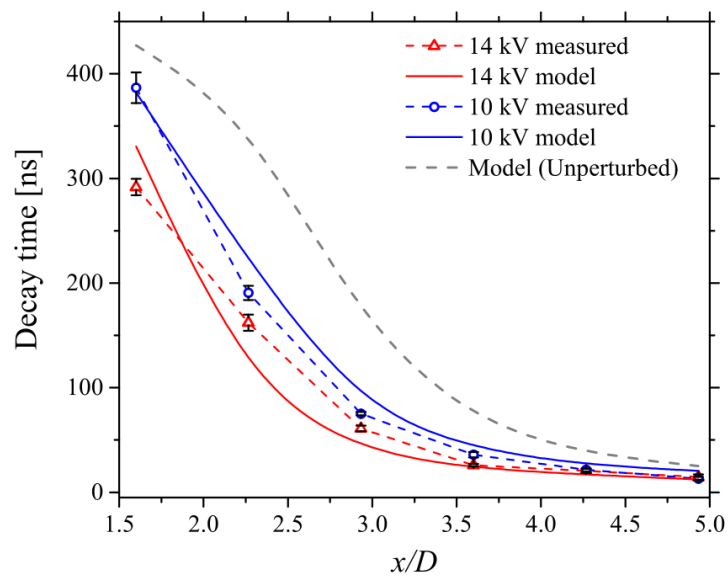


Figure 5. Comparison between measured and calculated decay time of the laser-induced fluorescent signal as a function of downstream distance from the jet orifice.

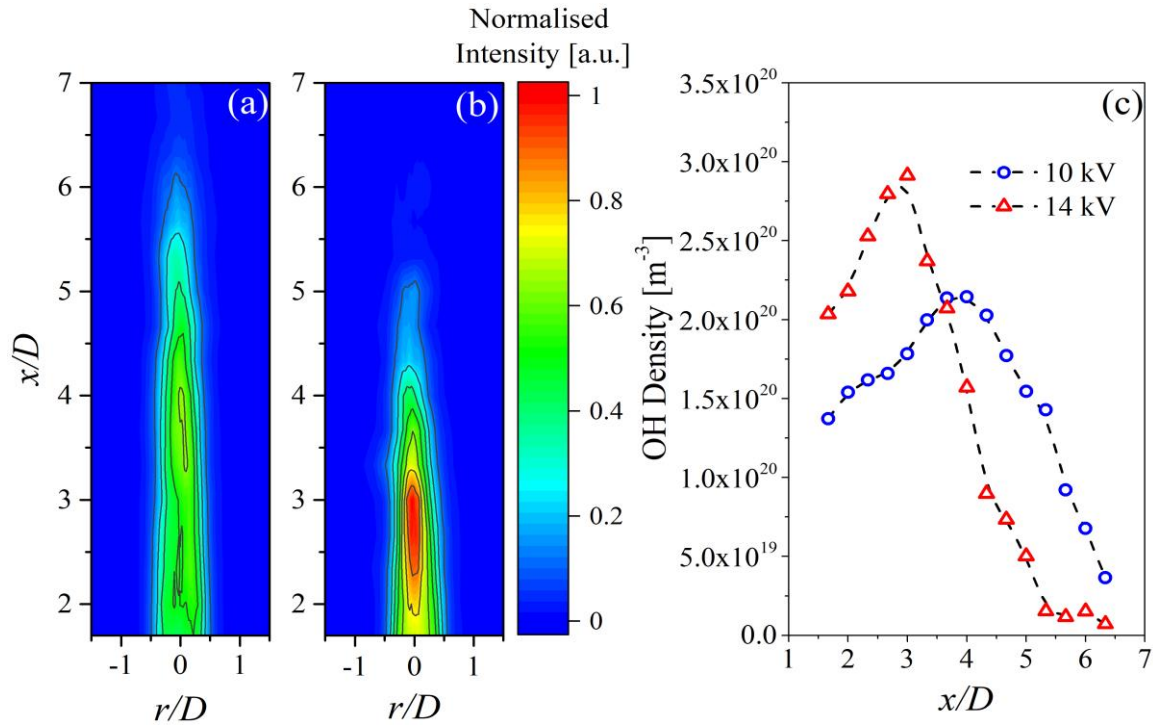
Using the experimental procedure outlined in section 2.2, the 2D LIF emission profile was compiled for both the 10 kV and 14 kV case and is shown in **Figure 6(a)** and **6(b)**, respectively. By comparing the centerline LIF intensity obtained from the 2D profile and the computed LIF intensity from the collisional radiative model, the absolute ground state OH density was calculated as a function of downstream position from the jet exit, shown in Figure 6(c). Consistent with the observations made in many previous studies, an increase in applied voltage was observed to increase the peak OH density within the plasma plume.^[26] Given that hydrogen-based species

densities increase when the air/water vapor fraction increases,^[48] it becomes likely that an increase in the applied voltage results in an increase in OH density as a result of not only more intense discharge conditions but also increased entrainment of air and H₂O. Critically, the position of peak OH density was found to vary depending on the applied voltage. This phenomenon is attributed to the interplay between the physical properties of the plasma (*i.e.*, n_e and T_e) and the fluid dynamics of the helium jet. With an applied voltage of 14 kV, perturbations within the jet shear layer caused by plasma generation induce an early transition to a turbulent flow regime, as confirmed in Figure 3 and 4. Under such conditions, the generation of OH close to the jet exit is locally enhanced due to enhanced H₂O entrainment combined with the relatively intense discharge conditions. Beyond the local maxima, the elevated air mole fraction as a result of the enhanced entrainment acts to quench the discharge and thus impedes OH generation. Conversely, at the lower applied voltage of 10 kV the discharge is comparatively less intense, meaning less air entrainment and a weaker plasma is formed, both factors contributing to limit OH production. However, less shear layer perturbation causes less air entrainment into the helium flow; thus, the discharge can propagate further from the orifice. Consequently, the concentration of ground-state OH is significantly higher far downstream from the jet exit in the 10 kV case compared to the 14 kV case.

The presented findings have considerable implications from a practical perspective as it has been demonstrated that the density of OH at a given downstream position is strongly influenced by both the discharge characteristics and its interaction with the quiescent background gas. While it is generally assumed that a higher plasma generation voltage results in enhanced production of OH, Figure 6 clearly shows that this only holds true close to the jet orifice. With increasing voltage comes increasing entrainment, which ultimately begins to quench the discharge and negatively affects downstream OH production. Counterintuitively, Figure 6(c) indicates that at a position of 5.3 x/D (*i.e.*, 16 mm from the jet exit), there is an order of magnitude more OH from a plasma generated using 10 kV compared to one generated using 14 kV excitation. These findings

438 demonstrate that the complex interplay between the physicochemical properties of the plasma and
 439 the fluid dynamic properties of the flowing noble gas must be carefully considered when designing
 440 plasma jet sources for use in applications such as biomedicine and materials processing.

441



442

443 **Figure 6.** Composite 2D normalized LIF intensity for (a) 10 kV, and (b) 14 kV case. Absolute
 444 centerline OH density for the 10 kV and 14 kV case as a function of distance from the jet orifice.

445

446 4 Conclusion

447 This contribution has employed Particle Image Velocimetry, Laser-Induced Fluorescence, and
 448 Computational Fluid Dynamics to explore the interplay between the propagating plasma plume and
 449 the quiescent background air in an axisymmetric dielectric barrier discharge jet. Despite the rapid
 450 onset of turbulence observed following plasma ignition, it was demonstrated that the presence of the
 451 plasma had little impact on the jet exit velocity of the helium flow. Through statistical analysis of
 452 the measured velocity field from the plasma jet under varying excitation conditions, it was
 453 determined that plasma generation resulted in shear layer perturbations that grow downstream to
 454 initiate the early onset of turbulence.

455

456 Using the experimentally derived eddy viscosity, a computational model was developed to calculate
457 the density of humid air entrained within the helium jet flow. To validate the model, the calculated
458 decay time of the laser-induced fluorescent state of OH was compared against those measured
459 experimentally and found to be in good agreement. Finally, the computational model was used to
460 convert the measured LIF intensity into an absolute OH density from which it was concluded that
461 OH production is strongly influenced by the interplay between the propagating plasma and the
462 background air. At high applied voltages, it was found that OH density increases close to the exit
463 but is rapidly reduced downstream as a result of the elevated air content quenching the discharge.

464

465 In summary, this study demonstrates an intricate link between the physicochemical properties of the
466 plasma and its interaction with the quiescent air. As many applications rely on the presence of
467 reactive oxygen and nitrogen species, which are predominantly formed when the plasma interacts
468 with the background environment, the results of this study provide valuable insight into the
469 underpinning mechanisms governing these interactions.

470

471 **Acknowledgments:** JLW & MIH would like to acknowledge the support of the Engineering and
472 Physical Sciences Research Council (Projects EP/S025790/1, EP/S017623/1, EP/R041849/1, and
473 EP/N021347/1). RDW would like to acknowledge the support of the NATO AVT-254 plasma flow
474 control group.

475

476 **Keywords:** LIF; PIV; plasma; turbulence.

477 [1] A. J. Knoll, P. Luan, A. Pranda, R. L. Bruce, G. S. Oehrlein, *Plasma Process Polym.* **2018**, *15*,
478 1700217. doi.org/10.1002/ppap.201700217

479 [2] X. Deng, A. Yu Nikiforov, T. Coenve, P. Cools, G. Aziz, R. Morent, N. De Geyter, C. Leys,
480 *Sci. Rep.*, **2015**, *5*, 10138. doi.org/10.1038/srep10138

- 481 [3] P. B. Flynn, S. Higginbotham, N. H. Alshraiedeh, S. P. Gorman, W. G. Graham, B. F. Gilmore,
482 *Int. J. Antimicrob. Agents*, **2015**, 46, 1. doi.org/10.1016/j.ijantimicag.2015.02.026
- 483 [4] H. Tanaka, M. Mizuno, K. Ishikawa, S. Toyokuni, H. Kajiyama, F. Kikkawa, M. Hori, *Plasma*,
484 **2018**, 1, 1. doi.org/10.3390/plasma1010014
- 485 [5] S. Bekeschus, P. Favia, E. Robert, T. Von Woedtke, *Plasma Process Polym.*, **2019**, 16,
486 1800033. doi.org/10.1002/ppap.201800033
- 487 [6] S. Iseni, A. Schmidt-Bleker, J. Winter, K-D. Weltmann, S. Reuter, *J. Phys. D. Appl. Phys.*,
488 **2014**, 47, 152001. doi.org/10.1088/0022-3727/47/15/152001
- 489 [7] T. Darny, J. M. Pouvesle, J. Fontane, L. Joly, S. Dozias, E. Robert, *Plasma Sources Sci.*
490 *Technol.*, **2017**, 26, 105001. doi.org/10.1088/1361-6595/aa8877
- 491 [8] R. D. Whalley, J. L. Walsh, *Sci. Rep.*, **2016**, 6, 31756. DOI:10.1038/srep31756
- 492 [9] R. Xiong, Q. Xiong, A. Yu Nikiforov, P. Vanraes, C. Leys, *J. Appl. Phys.*, **2012**, 112, 033305.
493 DOI:10.1063/1.4746700
- 494 [10] M. Boselli, V. Colombo, E. Ghedini, M. Gherardi, R. Laurita, *Plasma Chem. Plasma Process.*,
495 **2014**, 34, 853. DOI:10.1007/s11090-014-9537-1
- 496 [11] S. Park, U. Cvelbar, W. Choe, S. Y. Moon, *Nat. Commun.*, **2018**, 9, 371. DOI:10.1038/s41467-
497 017-02766-9
- 498 [12] M. I.Hasan, J. W. Bradley, *J. Phys. D: Appl. Phys.*, **2016**, 49, 055203. DOI:10.1088/0022-
499 3727/49/5/055203
- 500 [13] A. Michalke, *Journal of Fluid Mechanics*, **1965**, 23, 3. DOI:10.1017/S0022112065001520
- 501 [14] M. Lessen, *Nat. Adv. Comm. Aero., Wash.*, **1950**, 979.
- 502 [15] A. Michalke, *J. Fluid Mech.*, **1965**, 23, 3. DOI:10.1017/S0022112065001520
- 503 [16] A. Michalke, R. Wille, *Proc. 11th Intern. Congr. Appl. Mech.*, **1965**.
- 504 [17] A. Michalke, *Prog. Aerosp. Sci.*, **1972**, 12, 213. DOI:10.1016/0376-0421(72)90005-X
- 505

506 [18] A. V. Pipa, T. Bindemann, R. Foest, E. Kindel, J. Röpcke, K-D. Weltmann, *J. Phys. D. Appl.*
507 *Phys.*, **2008**, *41*, 194011. DOI:10.1088/0022-3727/41/19/194011

508 [19] K. McKay, J. S. Oh, J. L. Walsh, J. W. Bradley, *J. Phys. D. Appl. Phys.*, **2013**, *46*, 464018.
509 DOI:10.1088/0022-3727/46/46/464018

510 [20] A. Schmidt-Bleker, J. Winter, S. Iseni, M. Dünnbier, K-D. Weltmann, S. Reuter, *J. Phys. D.*
511 *Appl. Phys.*, **2014**, *47*, 145201. DOI:10.1088/0022-3727/47/14/145201

512 [21] D. Riès, G. Dilecce, E. Robert, P. F. Ambrico, S. Dozias, J. M. Pouvesle, *J. Phys. D. Appl.*
513 *Phys.*, **2014**, *47*, 275401. DOI:10.1088/0022-3727/47/27/275401

514 [22] S. Reuter, J. Winter, A. Schmidt-Bleker, D. Schroeder, H. Lange, N. Knake, V. Schulz-Von
515 Der Gathen, K. D. Weltmann, *Plasma Sources Sci. Technol.*, **2012**, *21*, 024005. DOI:10.1088/0963-
516 0252/21/2/024005

517 [23] A. Nikiforov, L. Li, N. Britun, R. Snyders, P. Vanraes, C. Leys, *Plasma Sources Sci. Technol.*,
518 **2014**, *23*, 015015. DOI:10.1088/0963-0252/23/1/015015

519 [24] C. Tropea, A. L. Yarin, J. F. Foss, *Springer Handbook of experimental fluid mechanics*,
520 Springer, NY, USA **2007**.

521 [25] L. Li, A. Nikiforov, Q. Xiong, N. Britun, R. Snyders, X. Lu, C. Leys, *Phys. Plasmas*, **2013**, *20*,
522 093502, DOI: 10.1063/1.4820945),

523 [26] S. Yonemori, R. Ono, *J. Phys. D: Appl. Phys.*, **2014**, *47*, 125401, DOI:10.1088/0022-
524 3727/47/12/125401

525 [27] J. Vorac, P. Dvorak, V. Prochaska, J. Ehlbeck, S. Reuter, *Plasma Sources Sci. Technol.*, **2013**,
526 *22*, 025016, DOI:10.1088/0963-0252/22/2/025016

527 [28] T. Verreycken, R. M. Van Der Horst, N. Sadeghi, P. J. Bruggeman, *J. Phys. D. Appl. Phys.*,
528 **2013**, *46*, 464004. DOI:10.1088/0022-3727/46/46/464004

529 [29] G. Dilecce, L. M. Martini, P. Tosi, M. Scotoni, S. De Benedictis, *Plasma Sources Sci.*
530 *Technol.*, **2015**, *24*, 034007. DOI:10.1088/0963-0252/24/3/034007

531 [30] YF. Yue, XK. Pei, XP. Lu, *IEEE Trans. Radiat. Plasma Med. Sci.*, **2017**, *1*, 6. DOI:
532 10.1109/TRPMS.2017.2757037

533 [31] R. J. Kee, M. E. Coltrin, P. Glarborg, *Chemically reacting flow: theory and practice*, Wiley-
534 Interscience, Hoboken, NJ, USA **2003**. DOI:10.1002/0471461296

535 [32] R. B. Bird, W. E. Stewart, E. N. Lightfoot, *Transport Phenomena*, 2nd edition, John Wiley &
536 Sons, NY, USA **2002**.

537 [33] S. P. Wasik, K. E. McCulloh, *J. Res. Natl. Bur. Stand.*, **1968**, 73A, 2.

538 [34] J. Rohling, J. Shen, C. Wang, J. Zhou, C. E. Gu, *Appl. Phys. B*, **2007**, 87, 355.
539 DOI:10.1007/s00340-007-2595-9

540 [35] C. V. Paganelli, F. K. Kurata, *Respiration Physiology*, **1977**, 30, 15. DOI:10.1016/0034-
541 5687(77)90018-4

542 [36] T. J. Chung, *Computational fluid dynamics*, Cambridge University Press, Cambridge, UK
543 **2002**.

544 [37] D. Xu, J. Chen, *Exp. Therm. Fluid Sci.*, **2013**, 44 662.
545 DOI:10.1016/j.expthermflusci.2012.09.006

546 [38] C. Gualtieri, A. Angeloudis, F. Bombardelli, S. Jha, T. Stoesser, *Fluids*, **2017**, 2, 17.
547 DOI:10.3390/fluids2020017

548 [39] M. Boselli, V. Colombo, M. Gherardi, R. Laurita, A. Liguori, P. Sanibondi, E. Simoncelli, A.
549 Stancampiano, *IEEE Trans. Plasma Sci.*, **2015**, 43, 3. DOI: 10.1109/TPS.2014.2381854

550 [40] H. Sato, *J. Phys. Soc. Jpn.*, **1956**, 11, 702. DOI:10.1143/JPSJ.11.702

551 [41] H. Sato, *J. Phys. Soc. Jpn.*, **1959**, 14, 1797. DOI:10.1143/JPSJ.14.1797

552 [42] E. Gutmark, C-M. Ho, *Phys. Fluids*, **1983**, 26, 2932. DOI:10.1063/1.864058

553 [43] J. Cohen, I. Wygnanski, *J. Fluid Mech.*, **1987**, 176, 191. DOI:10.1017/S0022112087000624

554 [44] S. W. Rienstra, *J. Sound Vib.*, **1983**, 86, 4. DOI:10.1016/0022-460X(83)91019-2

555 [45] J. Westerweel, C. Fukushima, J.M. Pederson, J. C. R. Hunt, *Phys. Rev. Lett.*, **2005**, 95,
556 174501. DOI:10.1103/PhysRevLett.95.174501

- 557 [46] B. Lautrup, *Physics of continuous matter: exotic and everyday phenomena in the macroscopic*
558 *world*, Institute of Physics, Bristol, UK **2005**.
- 559 [47] S. Yonemori, Y. Nakagawa, R. Ono, T. Oda, *J. Phys. D. Appl. Phys.*, **2012**, 45, 225202.
560 DOI:10.1088/0022-3727/45/22/225202
- 561 [48] T. Murakami, K. Niemi, T. Gans, D. O'Connell, W. G. Graham, *Plasma Sources Sci. Technol.*,
562 **2013**, 22, 015003. DOI:10.1088/0963-0252/22/1/015003
- 563